IEEE Open Journal of Vehicular Technology

Received 3 January 2023; accepted 8 January 2023. Date of publication 16 January 2023;
date of current version 28 February 2023. The review of this article was coordinated by Editor Edward Kwok Shum Au.

Digital Object Identifier 10.1109/OJVT.2023.3237158

IEEE 802.11bf DMG Sensing: Enabling High-Resolution mmWave Wi-Fi Sensing

STEVE BLANDINO [1,2], TANGUY ROPITAULT [1,2], CLAUDIO R. C. M. DA SILVA [3] (Senior Member, IEEE), ANIRUDHA SAHOO [1] (Senior Member, IEEE), AND NADA GOLMIE [1] (Fellow, IEEE)

(Invited Paper)

[1]National Institute of Standards and Technology, Gaithersburg, MD 20899 USA
[2]Prometheus Computing LLC, Cullowhee, NC 28723 USA
[3]Reality Labs, Meta Platform, Redmond, WA 98052 USA

CORRESPONDING AUTHOR: STEVE BLANDINO (e-mail: steve.blandino@nist.gov).

ABSTRACT IEEE 802.11bf amendment is defining the wireless Local Area Network (WLAN) sensing procedure, which supports sensing in license-exempt frequency bands below 7 GHz, and the Directional Multi-Gigabit (DMG) sensing procedure for license-exempt frequency bands above 45 GHz. In this paper, we examine the use of Millimeter-Wave (mmWave) Wi-Fi to enable high-resolution sensing. We first provide an introduction to the principle of sensing and the modifications defined by the IEEE 802.11bf amendment to IEEE 802.11 to enable mmWave Wi-Fi sensing. We then present a new open-source framework that we develop to enable the evaluation of the DMG sensing procedure accuracy. We finally quantify the performance of the DMG sensing in terms of the velocity/angle estimate accuracy, and its overhead on the communication link. Results show that the DMG sensing procedure defined in IEEE 802.11bf is flexible enough to accommodate a wide range of sensing applications. For the bistatic scenario considered, the velocity accuracy is in the interval 0.1 m/s to 0.4 m/s, while the angular accuracy is between 1° and 8 degrees depending on the sensing parameters used. Ultimately, the overhead introduced by sensing is limited with a sensing overhead below 5.5% of the system symbol rate.

INDEX TERMS Millimeter wave communication, radar remote sensing, IEEE standards activities, open source software.

I. INTRODUCTION

Future wireless networks are envisioned to augment communication operations with sensing capabilities [1], [2]. Integrating sensing and communication is attractive thanks to its potential benefits, such as more efficient spectrum and hardware utilization, optimized resource allocation and the support of a number of sensing services, including human activity and gesture recognition in smart homes. In addition, in-vehicle sensing has recently gained traction promising safety enhancements with applications such as driver sleepiness detection and reckless driving recognition in smart vehicles [3].

Wi-Fi networks, both in the licence-exempt frequency bands below 7 GHz and in the Millimeter-Wave (mmWave) above 45 GHz, are the perfect candidates to implement sensing features using existing communications infrastructures and enabling coordination between multiple devices. Sensing through Wi-Fi networks aims at utilizing Wi-Fi signals to detect and sense targets, such as people, animals, objects, and/or locations of interest. While the feasibility of using Wi-Fi to enable sensing has been demonstrated over the past several years [4], [5], [6], [7], [8], [9], the range of applications that is currently supported is limited due to the lack of sensing-specific features in the IEEE 802.11 standard, hindering the usage of multiple 802.11 devices from different vendors for sensing applications. For this reason, Task Group IEEE 802.11bf (TGbf) started in September 2020 the development of an amendment to the IEEE 802.11 standard supporting sensing [10]. The main contribution of the IEEE 802.11bf amendment is the definition of the Wireless Local Area Network (WLAN) sensing procedure, which supports

sensing in license-exempt frequency bands below 7 GHz (2.4 GHz, 5 GHz, and 6 GHz), and its mmWave (above 45 GHz) counterpart, the Directional Multi-Gigabit (DMG) sensing procedure, which is the focus of this paper.

Despite conceptual similarities in their operating mode, the definition of two distinct sensing procedures is necessary because of unique propagation, bandwidth, and hardware characteristics. For instance, to satisfy the link budget and provide sufficient coverage, DMG and Enhanced Directional Multi-Gigabit (EDMG) devices use Phased Antenna Arrays (PAAs). PAAs may synthesize pencilbeams – beams with a beamwidth of just a few degrees – dictating the direction of the propagation. The smaller the beamwidth, the easier to distinguish two targets apart. Hence, mmWave Wi-Fi has a superior spatial resolution compared to Wi-Fi, because of its integration capability to equip large PAAs on a single chip and also thanks to its large signal bandwidth. Thus, mmWave Wi-Fi enables use-cases requiring high spatial resolution, for instance, discriminating fingers in a gesture recognition application or obtaining reliable heart rate sensing for in-vehicle vital sign monitoring.

IEEE 802.11bf aims to reuse existing features of the IEEE 802.11ad and the IEEE 802.11ay standards [11], [12], which define the DMG and EDMG Physical Layers (PHYs), respectively. For instance, to guarantee uniform coverage overcoming the intrinsic directional properties of PAAs, IEEE 802 standard defines Training (TRN) sequences and the beam refinement protocol (BRP), enabling the estimation of the channel in different directions and thus potentially enabling the detection of targets in the environment. While these mechanisms can be repurposed to some extent, some modifications need to be introduced to facilitate a sensing framework, for example, specifying that the channel sounding aims at performing sensing measurements, extending the Beam Refinement Protocol (BRP) for multiple users and enabling the report of sensing measurements. An overview of IEEE 802.11bf is given in [13], presenting simulation results to quantify the impact of quantization on the quality of the channel state information report in the sub 7 GHz bands, however, to the best of our knowledge, our contribution is the first one to not only present the main definition and features of IEEE 802.11bf to enable high-resolution mmWave WiFi sensing, but also providing simulation results to quantify the sensing accuracy achievable with the DMG and EDMG PHYs of IEEE 802.11bf and the overhead on the data transmission. Moreover, we study the main trade-offs between sensing overhead and sensing accuracy and the flexibility provided by the DMG sensing procedure defined in IEEE 802.11bf to solve these trade-offs.

The remainder of this article is organized as follows. Section II introduces the principles of radar and directional sensing. Section III describes the DMG sensing procedure defined by IEEE 802.11bf to perform sensing in the mmWave band. Section IV describes the link level simulation platform developed to evaluate the DMG sensing. Section V provides the performance evaluation results of the sensing accuracy and sensing overhead as well as shedding light on the accuracy versus overhead trade-off. Finally, Section VI summarizes the contributions and the main findings of the paper.

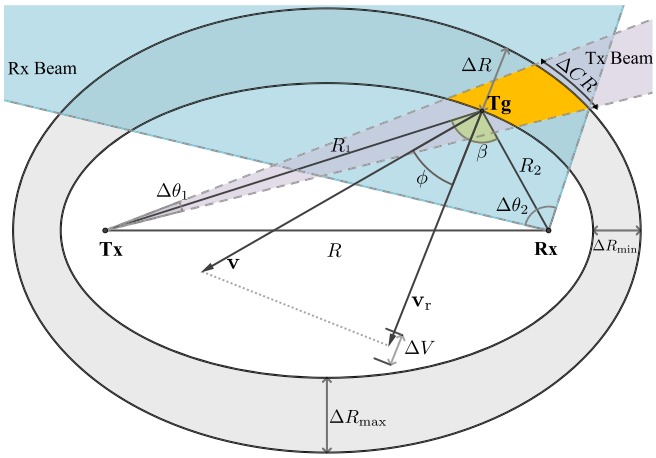

FIGURE 1. Generic radar remote sensing geometry.

II. PRINCIPLE OF RADAR REMOTE SENSING

In this section, principles of radar and directional sensing are reviewed [14], [15], [16], [17] to motivate IEEE 802.11bf's support of sensing applications. Specifically, the fundamental radar design parameters and measurements are described.

A generic system geometry is shown in Fig. 1 and considers transmitter (Tx) and receiver (Rx) spatially separated in a bistatic configuration. The path of length R connecting Tx and Rx is known as the bistatic baseline, and the angle β formed by the Tx to target range R_1 and target to Rx range R_2 is known as the bistatic angle. The basic function of a radar is to measure the time delay of the transmit signal within the main propagation beam of the Tx and the main propagation beam of the Rx, i.e., the time for a signal to travel a distance R_1 to reach a target, plus the time for the scattered signal, generated from the target, to travel a distance R_2 to reach the Rx. From the measured delay, the bistatic range $R_1 + R_2$ is computed. Another fundamental measurement that can be derived from the range measurement is the target velocity. To estimate the velocity, a radar system obtains consecutive measurements over a time window to detect variation of the range. Moreover, the use of pencil-beam antenna patterns enabled by PAAs for the transmission and reception of signals enables the estimation of the angular position of the target using the steering angles of the Tx/Rx beams combination.

Range, angle, and velocity measurements resolution are constrained by transceiver capabilities; the resolution of a radar can be defined as its ability to separate different targets in range, angle, or velocity. In the following, radar measurements and relative resolutions are discussed.

A. RANGE

A fundamental metric of radar sensing systems is range resolution, which is a measure of the ability of a system to resolve

multiple targets in proximity. For determining the target range, it is possible to measure the time of flight of the reflected signal traveling the distance $R_1 + R_2$. The total range $R_1 + R_2$, defines an isorange ellipse on which the target is located. The foci of the ellipse coincide with the positions of the Tx and the Rx. The bistatic range resolution is defined as the separation, ΔR, between two isorange ellipsoid that can be resolved by the radar. The range resolution depends on the capability to discriminate delays, hence on the bandwidth of the transmit signal, and upon the target position. As illustrated in Fig. 1, the minimun separation between two isorange ellipsoids ΔR_{min} is obtained at the extended baseline and the maximum separation ΔR_{max} at the bisector of the baseline. The bistatic range resolution, ΔR, measured along the bisector of the bistatic angle of the inner ellipse, can be expressed as:

$$\Delta R = \frac{c}{2B\cos(\beta/2)}, \tag{1}$$

where c is the speed of light in vacuum and B is the signal bandwidth. The best range resolution can be achieved for a monostatic configuration when the Tx and the Rx are co-located, i.e., when $\beta = 0$. For a generic case, when $\beta \neq 0$, the range resolution depends also upon the relative position of the target to the Tx and Rx. For large values of β, i.e., when the target is close to the baseline, the range resolution degrades, until a complete loss of range resolution for $\beta = 180^\circ$. Hence, depending on the sensing topology, the range resolution may vary. Monostatic architectures are suitable to support high-range resolution applications, while bi-static architectures might achieve a coarser resolution due to dependency to their geometry. The resolution achieved with bi-static configurations can be improved by intelligently combining measurements obtained with multiple and diverse links, i.e., using multistatic architectures.

DMG/EDMG signals are defined with a 1.76 GHz bandwidth, which can be potentially extended with channel bonding. Assuming a 1.76 GHz signal bandwidth, the best range resolution that can be achieved is $\Delta R = 0.17$ cm, making mmWave Wi-Fi a fundamental technology to enable applications requiring high resolution and high accuracy recognition.

B. ANGLE

Spatial accuracy can be further improved using directional antennas, as targets can be solved also in azimuth and elevation angle. By combining the azimuth and elevation information at both Tx and Rx with the bistatic range, the target position can be estimated by intersecting the bistatic ellipse with the Tx and Rx main lobes' directions. The azimuth and the elevation angles of the target are determined by the pointing angle of the antenna main beam, when maximizing the power of the scattering signal of the target. The width of the main beam determines the angular resolution $\Delta\theta_i$ of the antenna, which is usually defined as the 3 dB antenna beamwidth. $\Delta\theta_1$ and $\Delta\theta_2$ refer to the angular resolution of the transmitter and receiver, respectively.

In a bistatic configuration, the minimum separation between two targets lying on the same isorange ellipse that can be discriminated by the radar in the angular domain, i.e., cross-range resolution, is usually defined by the beam with the narrower cross-range resolution. For example, assuming the transmit beam to be too large to contribute to the angular resolution as in Fig. 1, i.e., if $2R_2 \cdot \sin(\Delta\theta_2/2) \geq 2R_1 \cdot \sin(\Delta\theta_1/2)$, the cross-range resolution ΔCR can be defined as:

$$\Delta CR = \frac{2R_1 \cdot \sin(\Delta\theta_1/2)}{\cos(\beta/2)}. \tag{2}$$

In Fig. 1, the intersection between the range resolution area and the cross-range resolution defines the boundary of a rectangular spatial resolution cell. The assumption that the spatial resolution cell is defined by the narrower beam does not always holds and more complex and irregular cells may be created; a general exact expression does not exist but specific antenna patterns and geometry have been studied [18].

As for the range measurement, fixing the position of the target and the antennas configuration, the best cross-range resolution can be achieved for a monostatic configuration, i.e., when $\beta = 0$. However, the cross-range resolution also depends on the distance of the target from Tx and Rx, since the resolution improves when the range R_1 or R_2 is decreased. Considering a monostatic DMG Station (STA)[1] equipped with a uniform linear array of 32 antennas, the $\Delta\theta \sim 3^\circ$ beamwidth yields a cross-range resolution $\Delta CR = 0.03$ m when the target is 0.50 m away from the STA, and it increases to $\Delta CR = 0.10$ m when the target is 2 m away. Hence, such a device would be able to identify gestures and finger movements for ranges below 0.5 m, more coarse gestures, for instance head motion, for a range between 0.5 m and 2 m or recognize body movements and activities for a range longer than 2 m.

C. VELOCITY

Fig. 1 highlights the spatial resolution cell defined by the range limited resolution and the angle limited resolution. Two targets in the same cell cannot be resolvable in space, however, they could be still discriminated against if their radial velocity falls in two different velocity resolution bins.

Assuming that Tx and Rx are stationary, and the target is moving with velocity $\mathbf{v}$, the range rate can be obtained deriving the sum range over time:

$$\hat{v} = \frac{d}{dt}(R_1 + R_2) = 2|\mathbf{v}|\cos\phi\cos\beta/2 = 2|\mathbf{v}_r|\cos\beta/2, \tag{3}$$

where ϕ is the angle formed between the target velocity vector $\mathbf{v}$ and the bistatic bisector, and $|\mathbf{v}_r| = |\mathbf{v}|\cos\phi$ is the radial velocity equal to the projection of the target velocity vector on the bistatic bisector. It can be shown that the bistatic velocity resolution, ΔV, measured along the bisector of the bistatic

[1] "A STA is any MAC/PHY entity providing the IEEE 802.11 MAC services" [19], and includes both Access Points (APs) and non-AP STAs.

angle of the inner ellipse, can be expressed as:

$$\Delta V = \frac{\lambda}{2T_c \cos(\beta/2)}, \tag{4}$$

where T_c is the observation time, also known as Coherent Processing Interval (CPI) and λ the wavelength. As for the range resolution, the maximum velocity resolution can be achieved in monostatic configuration. The velocity resolution degrades as the target approaches the baseline, degenerating to a loss of resolution when the target is on the baseline.

D. DATA CUBE

Achieving a fine velocity resolution, which is key in applications such as gesture recognition and heart/breathing rate estimation, requires a long observation interval T_c, as described in (4). To improve velocity resolution in a pulse radar, usually, several pulses are transmitted with the antenna beams pointed in a fixed direction, as shown in Fig. 2(a), because the observation time of a single pulse might not be long enough to resolve the motion. In a pulsed radar the observation time is thus $T_c = I \cdot \Delta T$, I being the number of pulses and ΔT the pulse repetition interval. The pulse number is usually referred to as *slow time* domain. For each pulse, a series of echoes corresponding to different range bins are collected, in the *fast time* domain, as shown in Fig. 2(c) and (d). The Tx and Rx antenna arrays are electrically swept across different steering angles since the direction of the target is not known, and for each beam combination a sequence of pulses is sent. The response for each beam configuration is stored in the *beam* dimension. Hence, the radar return of each pulse is collected in a 3-dimensional matrix, shown in Fig. 2(b), including information of the range, evolution over time and antenna beams.

Doppler processing operates on the data cube to obtain information about the Doppler frequency shift ν, which is related to velocity $\hat{v}$ as $\nu = \hat{v}/\lambda$; coherent integration of the returns from many consecutive pulses can be performed using a discrete Fourier Transform; the discrete Fourier Transform compensates the Doppler phase shift introduced by the target motion and coherently sums the multiple measurements. Using multiple pulses improves the velocity resolution and increases the Signal-to-Noise Ratio (SNR), which benefits from the boost of the coherent integration gain. At the end of the Doppler processing, a range-Doppler (or velocity) map is obtained, as shown in Fig. 2(f).

III. DMG SENSING PROCEDURE

IEEE 802.11bf [10] amendment introduces Medium Access Control (MAC) and DMG/EDMG PHY modifications to support mmWave Wi-Fi sensing (i.e., sensing in the bands above 45 GHz). The *DMG sensing procedure* is in charge of mmWave Wi-Fi sensing and enables STAs to:

- inform other STAs of their sensing capabilities;
- request and setup transmissions that allow for sensing measurements to be performed;
- perform sensing measurements enabling Doppler processing, i.e., allow to transmit consecutive "pulses" at a given repetition interval. In 802.11 context, the "pulses" are PHY Protocol Data Units (PPDUs);
- exchange either raw or Doppler-processed sensing measurement results;
- release the resources allocated for sensing.

A. DMG SENSING PROCEDURE ROLES AND SUPPORTED SENSING

The DMG sensing procedure operates with two sets of roles. First, the STA initiating the sensing (i.e., the STA that supports the sensing application), is referred to as the *sensing initiator*, while the STAs participating to the sensing and responding to the sensing initiator are denoted as the *sensing responder(s)*. Then, the STA sending the PPDU used for sensing is designated as a *sensing transmitter* while a STA performing the sensing measurements using this PPDU is called as a *sensing receiver*.

The DMG sensing procedure supports the following sensing architectures: monostatic, bistatic, multistatic, monostatic sensing with coordination, bistatic sensing with coordination, and passive sensing. As shown in Fig. 3, these architectures can be differentiated based on the roles of each STA, and the number of devices used to obtain the sensing measurements. *Monostatic* architectures involve a single STA, which is both the sensing transmitter and sensing receiver (Fig. 3(a)). Monostatic sensing can support short-range high-resolution applications such as gesture recognition and sleep monitoring. When the measurements are made by a single sensing receiver using signals transmitted by a single sensing transmitter, which is not co-located with the sensing receiver, the architecture is said to be *bistatic* (Fig. 3(b)). Compared to monostatic architectures, bistatic architectures can support applications requiring a wider sensing area, such as people tracking in a room, and that may require lower-complexity implementations. When the sensing transmitter and more than one sensing receivers are distinct STAs (e.g., one sensing transmitter STA and two sensing receiver STAs), the architecture is said to be *multistatic* (Fig. 3(c)). Multistatic architecturse may offer a wider sensing range and better resolution and accuracy than bistatic architectures. Thus, multistatic sensing may support applications such as people counting and tracking in a home. *Coordinated monostatic* (Fig. 3(d))/*bistatic* (Fig. 3(e)) is an extension of monostatic/bistatic architecture, which allows coordinating more than one monostatic/bistatic sensing; the coordination is performed by the AP. The coordination aims to avoid collisions and optimize the spectrum utilization, and thus have no impact on range, resolution, and accuracy of the applications supported. Finally, IEEE 802.11bf defines *passive sensing* where the STAs receive PPDUs transmitted by one or more STAs that are not necessarily intended for DMG sensing, e.g., DMG Beacon frames (Fig. 3(f)). Since Beacon frames are sent using the smallest bandwidth supported and with a period that is relatively long for sensing applications, passive sensing is particularly adapted for sensing applications with lower-resolution requirements.

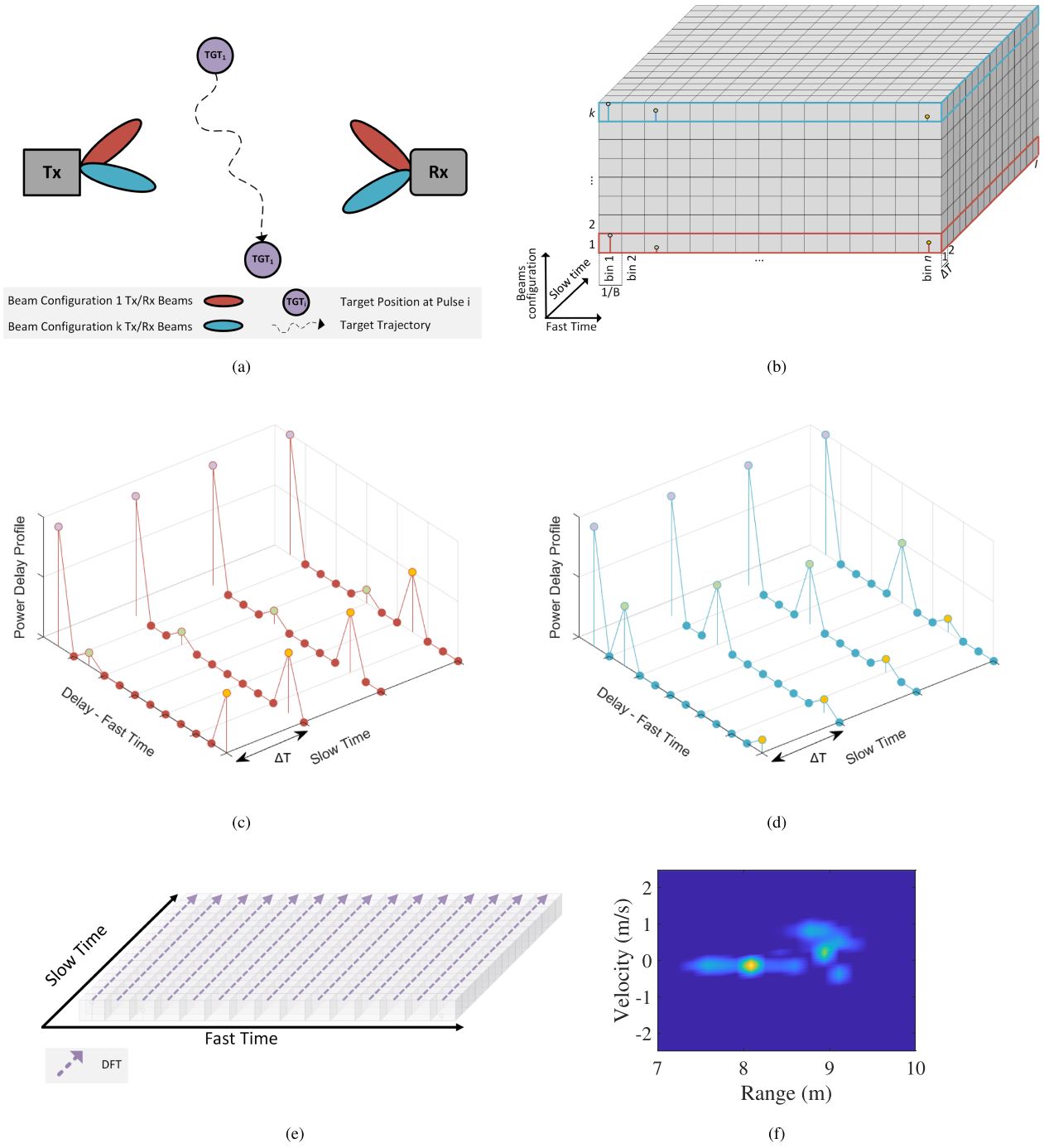

FIGURE 2. **Example of data cube measurement and Doppler Processing. (a) Example topology (b) Corresponding Data cube with *n* fast time bins, *I* slow time pulses and *k* beam configuration tested (c) Power Delay Profile for beam configuration 1 and first four slow time pulses (d) Power Delay Profile for beam configuration k and first four slow time pulses (e) DFT along the slow time axis to obtain the range Doppler map for a single beam configuration (f) Example of Doppler range map for a single beam configuration.**

For sensing types requiring more than one sensing responder, i.e., multistatic, coordinated monostatic or coordinated multistatic, the sensing initiator of a DMG sensing procedure must be an AP STA. Each of the different sensing types is addressed in [10] except monostatic. As monostatic sensing involves only one STA, it does not require any communication or coordination between multiple STAs and therefore is not specifically addressed in IEEE 802.11bf besides providing some constraints on the PPDU to use for monostatic sensing.

B. DMG SENSING PROCEDURES PHASES

As displayed in Fig. 4, the DMG sensing procedure is made of one or more of the following phases:

- DMG sensing session setup.

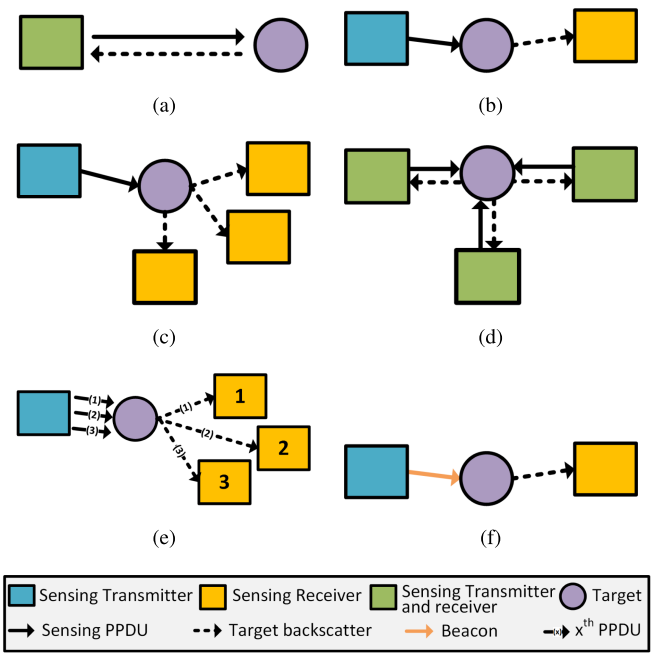

FIGURE 3. Supported DMG sensing types examples: (a) Monostatic. (b) Bistatic. (c) Multistatic. (d) Coordinated monostatic. (e) Coordinated bistatic. (f) Passive.

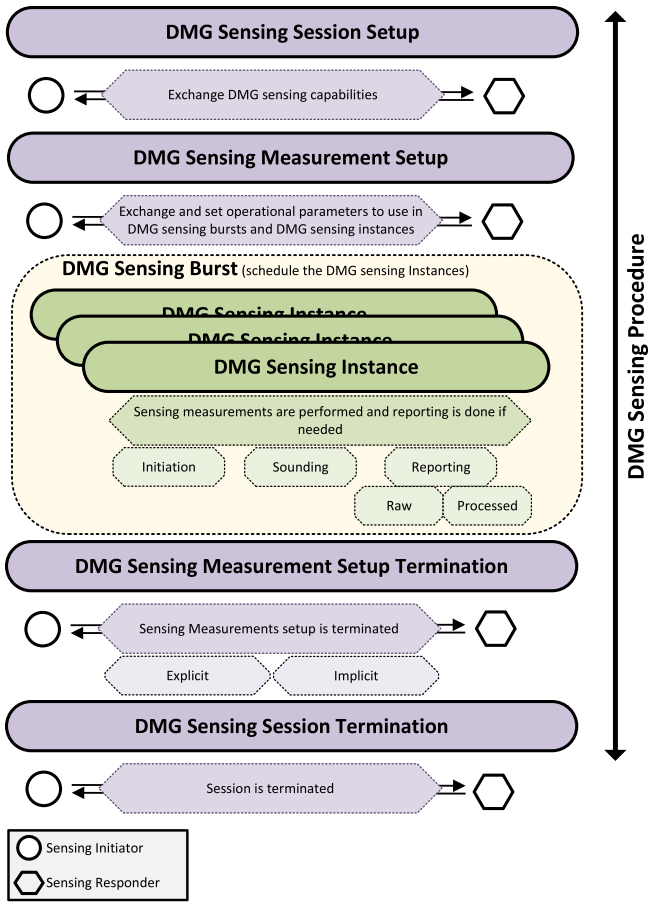

FIGURE 4. Overview of the DMG sensing procedure.

- DMG measurement setup.
- DMG sensing burst.
- DMG sensing instance.
- DMG measurement setup termination.
- DMG sensing session termination.

1) DMG SENSING SESSION SETUP

Not all 802.11 STAs will support sensing or all the sensing types and roles. Thus, the *DMG sensing session setup* allows a sensing initiator and a sensing responder to exchange DMG sensing capabilities such as the sensing type supported (e.g., bistatic, multistatic), the roles supported for a given sensing type (e.g., a STA supports to be sensing receiver for bistatic), or sensing reports type available (either raw Channel State Information (CSI) measurements or sensing processed results). The capabilities are exchanged using procedures commonly used in the IEEE 802.11 standard such as beaconing for AP and association for non-AP STA. The DMG session setup helps a sensing initiator to identify the potential STAs that can be used as sensing responder for a given sensing application with given requirements.

2) DMG MEASUREMENT SETUP

To configure the sensing parameters and STA roles for a given sensing application, the *DMG measurement setup* is used. It enables a sensing initiator and a sensing responder to exchange and agree on Operational Parameters (OPs) associated with DMG sensing bursts and DMG sensing instances (defined below). The OPs can include the sensing roles of the sensing initiator and the sensing responder(s), the DMG sensing type, the DMG burst configuration, the DMG measurement report types, and other parameters. The measurement setup is established with the initiator sending a *DMG Sensing Measurement Setup Request* frame to a responder, which replies with a *DMG Sensing Measurement Response frame* either accepting, rejecting or proposing new OPs to the sensing initiator. The sensing initiator repeats this process as many times as sensing responders involved in the DMG sensing procedure.

3) DMG SENSING BURST

IEEE 802.11bf organizes the DMG sensing measurements through *DMG sensing bursts* and *DMG sensing instances* as depicted in Fig. 5. The *DMG sensing burst* represents the channel access time dedicated to sensing measurements for a single Doppler processing, i.e., the measurements used to obtain a data cube as introduced in II.D. Each DMG sensing burst is made of one or more DMG sensing instances, which is the effective period of time where the measurements take place. Each DMG sensing instance includes one or more PPDUs where the PPDU used depends on the sensing type. The DMG sensing burst defines two scheduling parameters: the *intra-burst interval* and the *inter-burst interval*. The former defines the time between the beginning of two consecutive

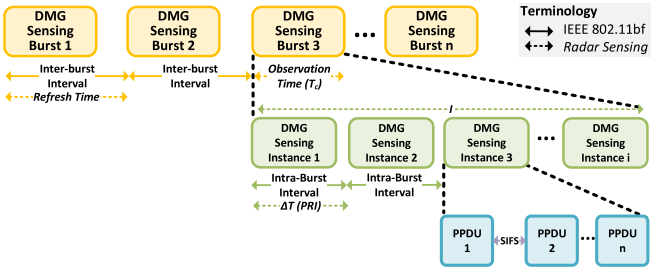

FIGURE 5. Organization of DMG Burst and DMG sensing instances.

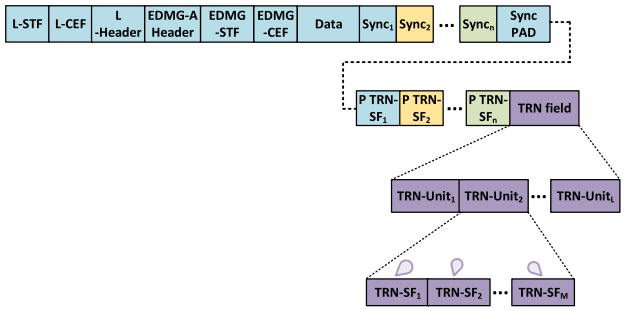

FIGURE 6. Multistatic PPDU structure for *n* sensing responders.

DMG sensing instances belonging to the same burst, while the latter is the time between the beginning of two consecutive bursts (i.e., the refresh time between two data cubes if the application requires more than one Doppler processing). As described in Section II.D, the computation of the Doppler frequency shift requires to collect I measurements every ΔT over a given observation time T_c. IEEE 802.11bf allows Doppler processing with the intra-burst interval being ΔT, the DMG sensing burst duration being the observation time T_c and the number of DMG sensing instances in a DMG sensing burst to be I.

4) DMG SENSING INSTANCE

Each DMG sensing instance belongs to a single DMG sensing burst and might possibly include the following phases: initiation phase, sounding phase, and reporting phase, the sounding phase being the only mandatory phase. The *initiation* phase allows a sensing initiator to check if the sensing responders participating in the DMG sensing procedure are available and also to configure information about the sounding (e.g., which sensing responder should perform the sounding first for a coordinated bistatic sensing). The initiation operates with the sensing initiator *sending DMG Sensing Request* frame to each responder which replies with a *DMG Sensing Response* frame. During the *sounding* phase, the sensing measurements are performed using PPDUs. Three different PPDUs are used depending on the sensing type:

- DMG/EDMG BRP PPDU as defined in IEEE 802.11ad/ay amendment [11] [12] for bistatic sensing and bistatic sensing with coordination. BRP PPDU are traditionally used to perform transmit (BRP-TX), receive (BRP-RX), or transmit/receive (BRP-RX/TX) beamforming training. To do so, TRN sequences (consisting of complementary Golay sequences) are appended to packets. The TRNs may be used to perform a fast angular scan covering different directions.
- The newly introduced EDMG multistatic sensing PPDU for multistatic sensing, extends the design of the BRP PPDU. This PPDU, as opposed to the legacy BRP PPDU, allows for multiple sensing receivers to perform sensing measurements using a single PPDU. The structure of multistatic sensing PPDU is shown in Fig. 6. The first change compared to an EDMG BRP PPDU structure is the insertion of a Sync field between the data field and the TRN field for each responder STA. The Sync field needs to be added as a multistatic PPDU is sent to a specific STA and thus beamformed for this STA. As a consequence, the other STAs might not be able to receive the preamble, header, and data part. Thus, each sync field is beamformed in the directions specific to each STA, and allows each STA to obtain accurate synchronization and to know where the intended TRN field starts. The second change is the presence of P TRN subfields per each responder STA, allowing each STA to track the phase and frequency. Finally, a Sync PAD subfield is introduced for legacy backward compatibility. These modifications allow for each responder to perform sensing measurements using the same PPDU.
- Monostatic PPDU for monostatic and monostatic with coordination sensing. Any DMG PPDU may be used for monostatic sensing but IEEE 802.11bf provides some constraints regarding to the waveform used in the TRN field portion of a PPDU used for monostatic sensing. These constraints are added to guarantee backward compatibility with legacy mmWave Wi-Fi devices and include constraints about the waveform length, transmission power, spectral density, and transmit mask.

Since passive sensing aims at performing sensing without allocating dedicated sensing resources, DMG passive sensing uses conventional PPDU such as the DMG beacon frames.

The reporting phase is in charge of exchanging the sensing measurements from the sensing receiver(s) to the sensing initiator. The reporting phase is mandatory only if the sensing responder is in the sensing receiver role or in the sensing transmitter and sensing receiver role. There are two types of reporting:

- "raw" results, i.e., the CSI results using the channel measurement feedback element. In this case, the sensing initiator receiving the report(s) will be in charge of the sensing processing. While the CSI allows for a precise characterization of the channel, the overhead resulting in the CSI report is large and can be detrimental to data communication. Thus, IEEE 802.11bf allows exchanging already processed sensing results.
- sensing processed results. The processing is done by the sensing receivers. There are two types of processed

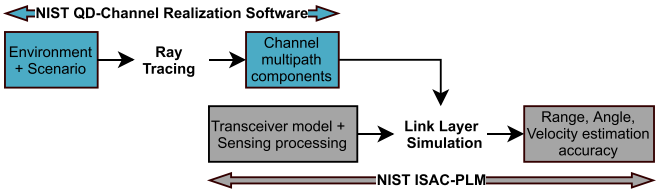

FIGURE 7. Overview of simulation platform.

reports: DMG sensing image report and DMG sensing targets report. *The DMG sensing image report* allows to return Doppler processed results (range, velocity or/and sensing transmitter/receiver angles) either in 2D, 3D, or 4D, the larger being the dimension, the larger being the overhead of the report. Thus, the DMG sensing image report, when configured to 4D, represents the doppler processing of the data cube depicted in Fig. 2(b) (fast time being the range, slow time being used for the Doppler, and beam configuration corresponding to the sensing transmitter/receiver angles) and a subset of the data cube when lower dimensions (2D or 3D) are configured. An example of 2D DMG sensing image using range and Doppler is shown in Fig. 2(f). The *DMG sensing targets report* processes the results one step further as it enables to return information per detected target (e.g., range, angle and velocity of each target), lowering the reporting overhead.

5) DMG MEASUREMENT SETUP TERMINATION AND DMG SENSING SESSION TERMINATION

The *DMG Sensing Measurement Setup Termination* and *DMG Sensing Session Termination* allow to release the sensing resources and are yet to be defined by TGbf.

IV. OPEN-SOURCE MODULAR SIMULATION PLATFORM

This section presents a novel open-source modular simulation platform, suited to simulate the DMG sensing procedure defined in IEEE 802.11bf. As shown in Fig. 7, the simulation platform integrates two modules, available as part of a collection of open-source tools to analyze WLAN mmWave network performance [20], [21].

The first module is the NIST Q-D channel realization software, i.e., a channel simulation software for Integrated Sensing And Communication (ISAC) applications [21], [22]. The second module is the NIST ISAC-PLM [23], which models the end-to-end IEEE 802.11ay PHY processing [24], including TRN-R and TRN-T fields enabling the evaluation of the DMG sensing procedure defined in IEEE 802.11bf.

The modular approach is adopted to allow flexibility to simulate and test a wide range of user requirements, as each of the modules can be easily replaced or extended. For instance, respecting the ISAC-PLM input interface, the channel model realization can be replaced with any other channel model implementation output or measurement campaigns output.

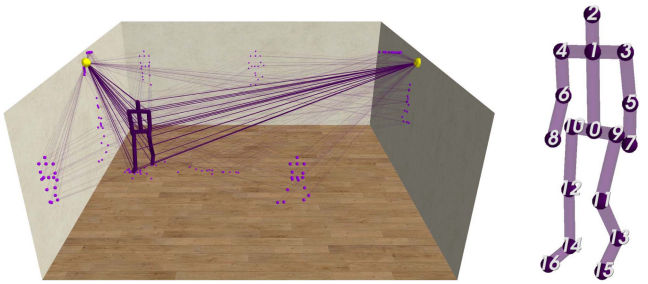

(a) T-rays ray tracing including direct backscattering and ghosts' reflections (b) Boulic Model

FIGURE 8. NIST Q-D channel realization software simulates multipath components generating from a human body model.

Conversely, the NIST Q-D channel realization software can be used with any custom signal processing implementations.

A. NIST Q-D CHANNEL REALIZATION SOFTWARE

The geometry of the environment and the topology of the scenario, e.g., position of the STAs and targets over time are defined in the NIST Q-D channel realization software, as shown in Fig. 8(a), depicting a single human target moving in an empty indoor environment. Using the ray tracing methodology, the channel multipath components (MPCs) are returned. The MPCs are a description of the amplitudes, delays and angles of arrival (AOA) and departure (AOD) of the multipath propagation channel. Some of the MPC models the radio signals reaching the Rx after interacting with the environment (*target unrelated MPCs*), others describe the interaction of the signal with the target (*target related MPCs*). The ray tracing of a moving scattering center enables space-time correlation of the scattered signal generating from the moving target. A complex target, i.e., a target composed of multiple scattering points, such as a human target can be modeled as a group of individual scattering centers distributed over the 3-dimensional space. In the NIST Q-D channel realization software, the target model used is a boulic model [25], shown in Fig. 8(b), which is a set of parameterized trajectories to represent the position of a human body in space. The model describes the motion of 17 joints (16 body segments) and each joint is considered as a scattering center of a human target.

B. NIST ISAC-PLM

The NIST ISAC-PLM module simulates an end-to-end EDMG PHY transmission. At the end of a DMG/EDMG PPDU or in an DMG/EDMG BRP packet, a sequence of Golay codes can be sent in a TRN field to train the receiver (TRN-R), the transmitter (TRN-T) or both (TRN-T/R). IEEE 802.11bf enables the possibility to re-use BRP frames for sensing purposes as well introducing a dedicated multi-static PPDU, also consisting of a sequence of TRN fields, as presented in Section III.B.

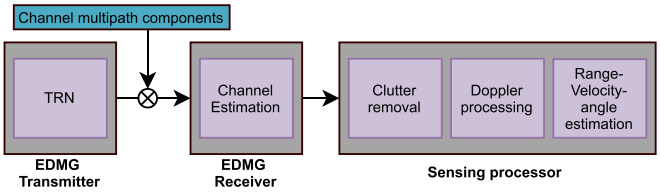

FIGURE 9. ISAC-PLM simulates the transmission of TRN fields to estimate target range, angle and velocity.

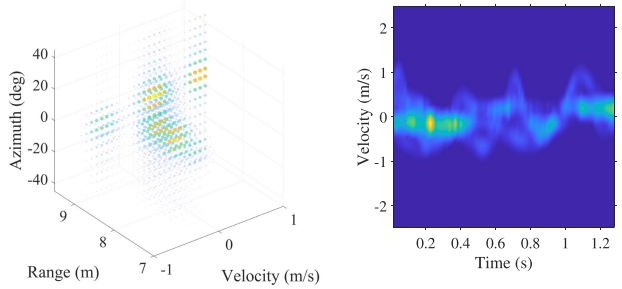

(a) Example of 3D DMG Sensing Image obtained using NIST-PLM

(b) Microdoppler spectrum.

FIGURE 10. Data cube processing in NIST-PLM.

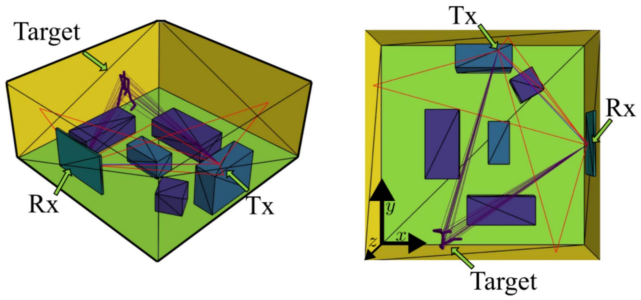

FIGURE 11. Simulation environment and bistatic geometry.

1) DMG PHY TRANSMISSION

ISAC-PLM simulates the transmission of a TRN field to evaluate the sensing performance when using directional communications, as shown in Fig. 9. The TRN field can be precoded using different Antenna Weight Vectors (AWVs), such that the sensing information can be extracted from the channel components that fall into the analog beam created by the selected AWVs. From a sensing perspective, the channel estimate can be seen as echoes from the targets and the environment. The delays of the echoes from the target MPCs are proportional to the bi-static distance. The channel estimate from consecutive the TRN sequences is collected in a 3-dimensional matrix including information about fast time, slow time, and angular domains.

2) DMG SENSING IMAGE

NIST ISAC-PLM construct a 3D DMG sensing image consisting of range, velocity and AOA or AOD azimuth and elevation, from which target parameters are derived. To obtain the 3D DMG sensing image, a discrete Fourier transform (DFT) is applied on the slow time dimension of the radar data matrix for each beam configuration, to obtain information about the Doppler frequency shift, which is proportional to the velocity of moving targets. Null Doppler values are considered as originating from static clutters, hence they are filtered out.

The obtained DMG sensing image is subject to a de-noise processing.

A threshold eliminating the noise floor and a low-pass filter with a 2D Gaussian window are applied to each beam configuration of the 2D range-Doppler image. After that, a peak detection algorithm is performed by comparing each pixel of the 2D DMG sensing range-Doppler image to its neighbors. If the tested pixel has a higher value than the surrounding pixels, the tested pixel is declared as a local maximum. The local maxima are thus retained in the de-noised DMG sensing image. An example of 3D DMG sensing image (range, the velocity, and the AOD azimuth) obtained with a DMG sensing burst, using NIST-PLM is shown in Fig. 10(a).

3) DMG SENSING TARGET PARAMETER

The estimation of the target properties, such as range, velocity and angle, is extracted from the DMG sensing image. To obtain the velocity estimation, DMG sensing images are summed over the range dimension and beam configuration, obtaining the microdoppler spectrum, shown in Fig. 10(b). The Doppler shift estimate is the point with the highest intensity in the microdoppler spectrum. Similarly, the estimation of AOA or AOD relies on the sum of the DMG sensing image over the Doppler and range domain, and the estimated angle is the highest value in the obtained angular spectrum.

V. DMG IEEE 802.11BF EVALUATION

In this section, we present simulation results in terms of sensing accuracy and overhead introduced by the sensing procedure on the communication link to evaluate the achievable performance of the DMG sensing procedure defined by IEEE 802.11bf and its flexibility to accommodate different sensing applications. The trade-off sensing accuracy-overhead is also discussed.

A. SENSING SCENARIO

We study a human motion detection application using a bistatic sensing architecture. The simulated environment is a room, shown in Fig. 11; the bottom left corner of the room is set as the coordinate origin. The sensing Tx is located at (4, 6.5, 1.6) m above a cabinet and the sensing Rx, on the TV screen, is located at (6.8, 3.5, 1.5) m. A human target is following a linear trajectory parallel to the y axis, completing a 1.3 m walk in a simulation time of 1.28 s. During the motion, the target creates a bistatic angle β in the interval between 39.8° and 42.5°. The living room is furnished, thus some of

the rays impinging on the target or generating from the target might be blocked by the furniture.

We consider that the sensing initiator is the sensing Rx; thus the Doppler processing is executed at the Rx and no reporting phase is required. The sensing Tx uses a PAA with isotropic radiators, while the receiver is an isotropic radiator; in this configuration, the Tx sends BRP-TX PPDUs precoded with different AWVs. To study the impact of the antenna pattern, several rectangular PAA sizes are simulated. We consider $A_v = 4$ vertical antenna elements, and we provide simulations for $A_h = 4,\ 8,\ 16$ horizontal antenna elements. As the beamwidth of the radiation pattern decreases with the number of antenna elements in the PAA, to measure the channel uniformly in the full search space, the entries N_{CB} of the PAA codebook scales with the antenna elements. We consider a codebook with a uniform sampling in the angular domain in both azimuth and elevation. To cover the full space, the codebook contains $N_{CB} = 81, 153, 297$ AWVs to test for 4×4, 4×8 and 4×16 antenna elements respectively. The maximum number of possible AWVs trained in the EDMG BRP-TX is given by $(M \cdot L)/N$, where M and N are the number of TRN subfields indicated in the EDMG TRN-Unit M field plus one and in the EDMG TRN-Unit N field plus one within the EDMG-Header-A of the packet, respectively. The TRN field is composed of a variable number L of TRN-Units, defined by the parameter EDMG TRN Length within the EDMG-Header-A of the packet. To precode the TRN field with all the entries of the codebook, the BRP packet is designed as $M = 16, N = 1$, and $L = 6, 10, 19$ for 4×4, 4×8, 4×16 respectively. The maximum number of AWVs that can be trained with these configurations are 96, 160 and 304, thus covering the entries of the designed codebooks.

To study the impact of the DMG sensing burst Intra-Burst Interval on sensing accuracy, several Intra-Burst Interval configurations are simulated. To keep the velocity resolution constant, the DMG sensing burst duration is fixed to T_c= 32 ms, while we provide simulations for $I = 4$, 8, 16, 32, and 64 DMG sensing instances per DMG sensing burst. Hence, the Intra-Burst Interval varies as $\Delta T = T_c/I$ =0.5, 1, 2, 4, and 8 ms. We set the Inter-Burst Interval equal to the Intra-Burst Interval. The Doppler FFT length is set to be twice the number of sensing instances per DMG sensing burst. The main design parameters are summarized in Table 1.

TABLE 1 Parameters of Simulated DMG IEEE 802.11bf Bistatic Sensing Architucture.

Parameter	*Value*					*Unit*
Signal bandwidth - B	1.76e9					Hz
Bistatic angle β	[39.77 - 42.47]					deg
Range resolution ΔR	0.09					m
Velocity resolution ΔV	0.10					m/s
Target velocity - $\|\mathbf{v}\|$	0.88					m/s
DMG sensing burst duration - T_c	32					ms
Packet type	BRP-TX					-
Golay Length - TRN_{BL}	128					-
EDMG TRN-Unit P - P	2					-
EDMG TRN-Unit M - $M-1$	15					-
EDMG TRN-Unit-N - $N-1$	0					-
Antenna dependent parameters						
Vertical PAA size A_v	4					-
Horizontal PAA size A_h	4	8	16			-
EDMG TRN Length - L	6	10	19			-
Codebook Size - N_{CB}	81	153	297			-
Max number of AWVs	96	160	304			-
Cross Range Resolution - ΔCR	2.9	1.5	0.75			m
Intra-Burst Interval dependent parameters						
Intra-Burst Interval - ΔT	0.5	1	2	4	8	ms
DMG Sensing Instances - I	64	32	16	8	4	-
Doppler FFT size	128	64	32	16	8	-

B. PERFORMANCE METRICS

The performance of the DMG sensing procedure is evaluated in terms of accuracy and overhead.

1) ACCURACY

In the following, we use the definition of accuracy as the absolute error $\epsilon_i = |\hat{x}_i - x_i|$, where $\hat{x}_i$ is the estimated parameter, x_i is the ground truth and i is the index of the observation. Moreover, to summarize the accuracy over the different observations, we use the definition of root mean square error (RMSE) defined as: $RMSE = \sqrt{1/K \sum_i^K \epsilon_i^2}$, being K the number of observations.

2) OVERHEAD

To evaluate the overhead of the sensing procedure on the symbol rate $f_c = 1.76 \cdot 10^9$ symbol per second (sps), we first compute the length of the EDMG BRP PPDU aiming at performing sensing measurements. The EDMG BRP PPDU length is:

$$L_{\text{BRP}} = L_{\text{DMG}} + L_{\text{EDMG}} + TRN_{BL} \cdot (P \cdot L \cdot (P + M)), \quad (5)$$

where $L_{\text{DMG}} = 4352$ symbols is the length of the legacy part of the DMG BRP PPDU (L-STF, L-CEF, L-Header) and $L_{\text{EDMG}} = 4608$ symbols is the length of the EDMG part of the EDMG BRP PPDU (EDMG-STF, EDMG-CEF). TRN_{BL} represents the length of the Golay sequence used in the TRN subfields. In this work, we use $TRN_{BL} = 128$. P is the value indicated by the EDMG TRN-Unit P field in the EDMG-Header A of the packet and in this work, we assume $P = 2$.

The sensing rate in sps is thus computed as:

$$f_{sens} = \frac{L_{\text{BRP}}}{\Delta T}. \quad (6)$$

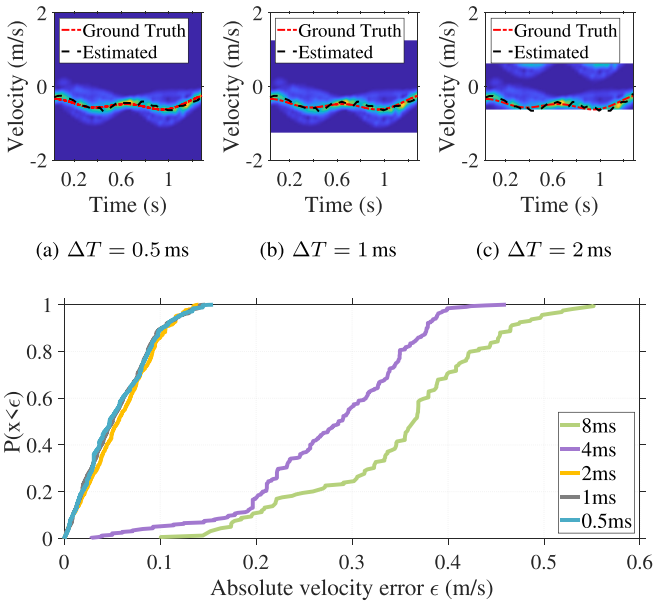

FIGURE 12. Impact of Intra-Burst Interval on velocity accuracy.

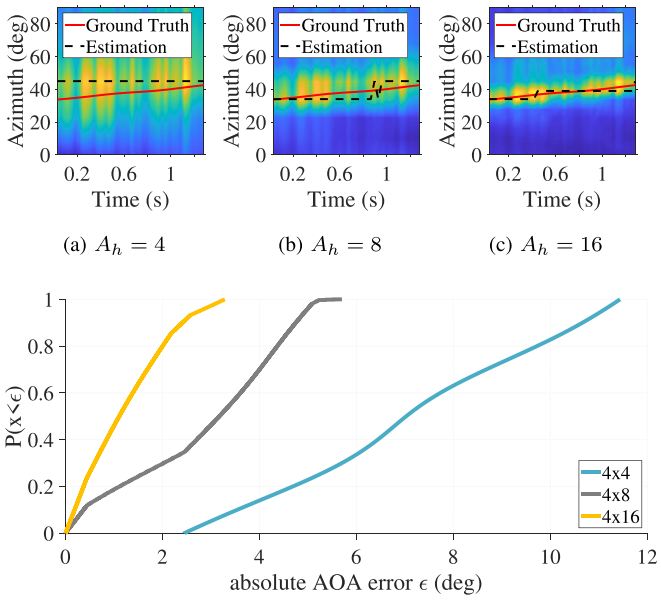

FIGURE 13. Impact of antenna pattern on angular estimation.

The antenna pattern and the codebook design influence f_{sens} with the length of the EDMG BRP-TX PPDU, since the number of TRN-T subfields in the EDMG BRP PPDU depends on the codebook size; the larger the codebook, the larger is the number of TRN-T subfields required. The Intra-Burst Interval determines how often the resources need to be allocated to sensing tasks.

Finally, to quantify the impact on the symbol rate, the overhead is computed by normalizing the sensing rate to the symbol rate, and expressed as a percentage as:

$$OH = f_{sens}/f_c \cdot 100. \tag{7}$$

C. EVALUATION OF SENSING ACCURACY

1) IMPACT OF INTRA-BURST INTERVAL ON SENSING ACCURACY

Fig. 12 shows the impact of different Intra-Burst Interval configurations on the velocity estimation. Fig. 12(a)-(c) show the microdoppler spectrum obtained with an Intra-Burst Interval set to 0.5 ms, 1 ms, 2 ms, respectively. Increasing the Intra-Burst Interval, the maximum velocity that can be detected decreases, as shown by the vertical span of the microdoppler spectrum. The configurations with a value of intra-burst interval of 0.5 ms and 1 ms, can detect a maximum velocity of 2.2 m/s and 1.1 m/s respectively, providing robustness to aliasing, as shown in Fig. 12(a) and (b). Instead, the configuration with a value of intra-burst interval of 2 ms, shows some aliasing, since the maximum velocity resolution is 0.6 m/s, while the speed of the target is around 0.88 m/s, as shown in Fig. 12(c). Despite the aliasing, the sensing processing is able to detect the target and estimate its velocity. Increasing the Intra-Burst Interval even further is not recommended for the considered scenario. Quantifying the error of the radial velocity estimation, Fig. 12(d) shows the cumulative density function of the velocity accuracy; a median accuracy of 0.05 m/s for Intra-Burst Interval smaller than 2 ms, while increasing the Intra-Burst Interval the accuracy error escalates, and a median error of 0.3 m/s and 0.4 m/s is observed for 4 ms and 8 ms respectively.

2) IMPACT OF ANTENNA PATTERN ON SENSING ACCURACY

Fig. 13 shows the impact of different PAA configurations on the AOA azimuth estimate. We omit the analysis of the elevation estimate as the target motion considered does not present any noticeable variation in the elevation plane. Fig. 13(a)-(c) show the azimuth spectrum varying the horizontal number of antennas as $A_h = 4$, 8 and 16. A larger beamwidth, such as the 4 horizontal antenna case, yields a lower angular resolution, a coarser azimuth spectrum, and a worse azimuth estimation. Increasing the number of antennas, i.e., increasing the angular resolution, the azimuth spectrum becomes sharper, and the azimuth estimation improves. The absolute azimuth error is quantified in Fig. 13(d). A median error of 1°, 3° and 7° is obtained for 4, 8 and 16 horizontal antennas respectively.

D. EVALUATION OF SENSING OVERHEAD

In this section, we quantify the overhead introduced by the sensing procedure and how it scales with the intra-burst interval and with the length of the EDMG BRP PPDU. Using the definition in (6) and in (7), Fig. 14 quantifies the overhead in both absolute value, i.e., sensing rate in Msps, and as a sensing overhead expressed as a fraction of the symbol rate. As expected, the sensing rate increases linearly with the Intra-Burst Interval, since halving the Intra-Burst Interval doubles

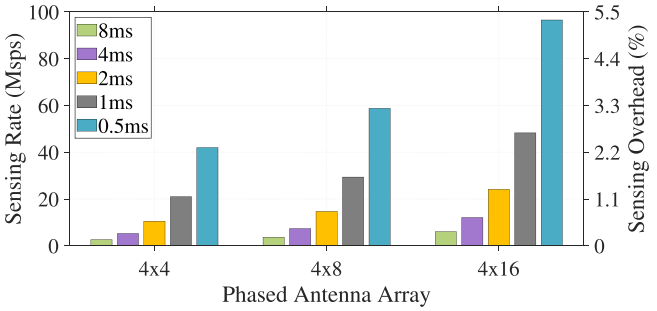

FIGURE 14. Sensing rate f_{sens} (Msps) and sening overhead *OH* (%) for different Intra-Burst Intervals and PAA size.

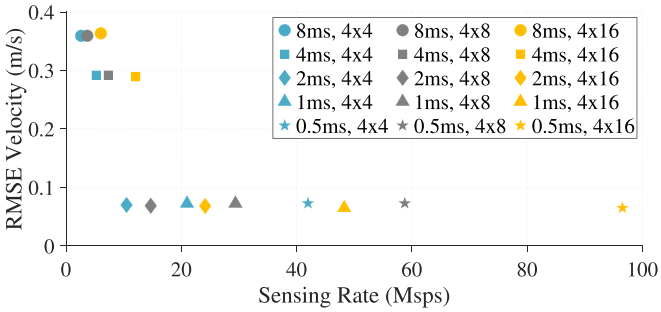

(a) Trade-off velocity accuracy-sensing rate

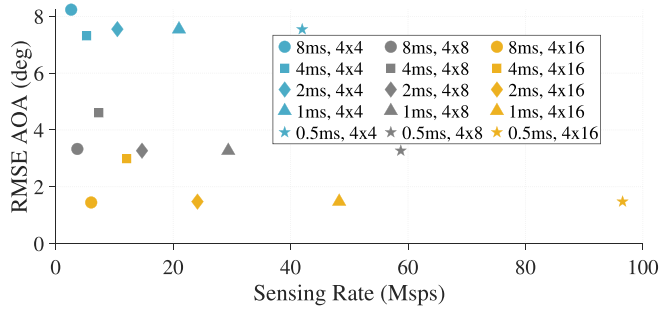

(b) Trade-off angular accuracy-sensing rate

FIGURE 15. Sensing overhead - sensing accuracy tradeoffs.

the overhead. The sensing rate also increases linearly with the size of the PAA, however with a smaller rate compared to the Intra-Burst Interval; for instance, increasing the antenna size from 8 to 16, the sensing overhead increases from 60 Msps to 90 Msps. This is explained by observing that while the TRN-T subfields portion of the EDMG BRP PPDU increases, the rest of the EDMG BRP PPDU remains constant in length. Fig. 14 also shows the impact of dedicated sensing packets on the communication rate. In the most demanding case considered, i.e., using an antenna array of 4×16 antenna elements and an Intra-Burst Interval $\Delta T = 0.5$ ms, the resources occupied by the sensing packets are below 5.5% of the symbol rate. The lowest overhead of 0.14% is achieved with ΔT =8 ms and a 4x4 antenna array.

E. SENSING ACCURACY VS OVERHEAD TRADEOFFS

To analyze the trade-offs between sensing accuracy and sensing resource requirements, we characterize the relationship between RMSE (velocity and azimuth AOA) and sensing rate, displaying the possible outcomes combining simulations with different Intra-Burst Intervals and different PAA antenna sizes.

1) TRADE-OFF VELOCITY ACCURACY - SENSING RATE

Fig. 15(a) shows the velocity RMSE over the sensing rate. The RMSE of the velocity estimation improves decreasing the Intra-Burst Interval, while the antenna pattern does not affect the trade-off. Hence, the trade-off velocity accuracy - sensing rate optimality is achieved with the smaller antenna pattern. Using a 4×4 PAA, the sensing rate is minimized using an Intra-Burst Interval $\Delta T = 8$ ms, while the RMSE is minimized using an Intra-Burst Interval $\Delta T = 2$ ms. The RMSE of the velocity estimation saturates when $\Delta T < 2$ ms. Thus, configurations with large antenna arrays (4×8 and 4×16) and small Intra-Burst Interval ($\Delta T < 2$) are inefficient to optimize the velocity estimation accuracy - sensing rate tradeoff.

2) TRADE-OFF ANGULAR ACCURACY - SENSING RATE

Fig. 15(b) shows the azimuth RMSE over the sensing rate. The RMSE AOA estimation improves, increasing the number of antennas, thanks to the smaller angular resolution. The Intra-Burst Interval does not affect the trade-off since the angular variation for a human walk is negligible when considering Intra-Burst Intervals in the order of milliseconds. Hence, optimality is achieved with the largest Intra-Burst Interval. Using $\Delta T = 8$ ms, the sensing rate is minimized using a 4x4 antenna pattern, while RMSE is minimized using the 4x16 antenna array. The configurations with faster Intra-Burst Interval are thus inefficient to optimize the angle estimation accuracy vs sensing rate tradeoff.

VI. CONCLUSION

IEEE 802.11bf amendment is defining the WLAN sensing procedure, which supports sensing in license-exempt frequency bands below 7 GHz, and the DMG sensing procedure for license- exempt frequency bands above 45 GHz. The discussion presented in this paper provides a concise introduction to the principles of sensing and how these principles are being integrated by the IEEE 802.11 MAC and DMG/EDMG PHY. We also provide an open-source framework, following the standard, to simulate its performance. In this paper we quantify the performance of the EDMG sensing procedure defined by IEEE 802.11bf in terms of sensing accuracy of velocity and angle estimation, and in terms of the overhead introduced by the sensing procedure. Based on an end-to-end simulation, we find that the DMG sensing procedure defined by IEEE 802.11bf provides a wide range of flexibility to accommodate different sensing applications. The RMSE of velocity can be adapted depending on the use case and we report a velocity accuracy in the interval 0.1 m/s to 0.4 m/s,

in the scenario considered. Similarly, the RMSE of the angle estimate can be adapted with the antenna array configuration and we measure an error between 1° and 8 degrees, in the scenario considered. The overhead introduced by sensing is kept under control, as in the simulated scenarios the overhead is always below 5.5% of the symbol rate of the system. Hence, a flexible accuracy-overhead trade-off can be solved based on the application requirements. As a future work, several open challenges remain to be studied. For example, the synchronization between transmitter and receiver is shared only for the monostatic case. In bistatic and multistatic, the Wi-Fi transceivers are not synchronized and the measured channel state information might exhibit phase distortions leading to a degradation of the sensing accuracy. Another open field of research requires the evaluation of the overhead generated by the DMG sensing procedure and its impact on the mmwave Wi-Fi communication as besides in passive mode, the DMG sensing procedure signaling is acting as a disruption of the Wi-Fi communication.

ACKNOWLEDGMENT

The authors would like to thank Assaf Kasher, Solomon Trainin, and Alecsander Eitan of Qualcomm Inc for constructive discussions and guidance.

REFERENCES

[1] C. De Lima et al., "Convergent communication, sensing and localization in 6G systems: An overview of technologies, opportunities and challenges," *IEEE Access*, vol. 9, pp. 26902–26925, 2021.

[2] J. Wang, N. Varshney, C. Gentile, S. Blandino, J. Chuang, and N. Golmie, "Integrated sensing and communication: Enabling techniques, applications, tools and datasets, standardization, and future directions," *IEEE Internet Things J.*, vol. 9, no. 23, pp. 23416–23440, Dec. 2022.

[3] X. Zeng, F. Wang, B. Wang, C. Wu, K. J. R. Liu, and O. C. Au, "In-vehicle sensing for smart cars," *IEEE Open J. Veh. Technol.*, vol. 3, pp. 221–242, 2022.

[4] S. Mosleh, J. B. Coder, C. G. Scully, K. Forsyth, and M. O. A. Kalaa, "Monitoring respiratory motion with Wi-Fi CSI: Characterizing performance and the BreatheSmart algorithm," *IEEE Access*, vol. 10, pp. 131932–131951, 2022.

[5] L. Storrer et al., "Indoor tracking of multiple individuals with an 802.11ax Wi-Fi-based multi-antenna passive radar," *IEEE Sensors J.*, vol. 21, no. 18, pp. 20462–20474, Sep. 2021.

[6] P. Falcone, F. Colone, A. Macera, and P. Lombardo, "Localization and tracking of moving targets with WiFi-based passive radar," in *Proc. IEEE Radar Conf.*, 2012, pp. 0705–0709.

[7] H. Abdelnasser, K. Harras, and M. Youssef, "A ubiquitous WiFi-based fine-grained gesture recognition system," *IEEE Trans. Mobile Comput.*, vol. 18, no. 11, pp. 2474–2487, Nov. 2019.

[8] C. Wu, F. Zhang, B. Wang, and K. J. Ray Liu, "mmTrack: Passive multi-person localization using commodity millimeter wave radio," in *Proc. IEEE Conf. Comput. Commun.*, 2020, pp. 2400–2409.

[9] F. Wang, F. Zhang, C. Wu, B. Wang, and K. J. R. Liu, "ViMo: Multiperson vital sign monitoring using commodity millimeter-wave radio," *IEEE Internet Things J.*, vol. 8, no. 3, pp. 1294–1307, Feb. 2021.

[10] *IEEE Draft Standard for Information Technology– Telecommunications and Information Exchange Between Systems Local and Metropolitan Area Networks– Specific Requirements Part 11: Wireless LAN Medium Access Control (MAC) and Physical Layer (PHY) Specifications Amendment 2: Enhancements for wireless LAN sensing*, IEEE p802.11bf/d0.5, 2022.

[11] *IEEE Standard for Information Technology–Telecommunications and Information Exchange Between Systems–Local and Metropolitan Area Networks–Specific Requirements-Part 11: Wireless LAN Medium Access Control (MAC) and Physical Layer (PHY) Specifications Amendment 3: Enhancements for Very High Throughput in the 60 GHz Band*, IEEE Standard 802.11ad-2012 (Amendment to IEEE Standard 802.11-2012, as amended by IEEE Standard 802.11ae-2012 and IEEE Standard 802.11aa-2012), 2012.

[12] *IEEE Standard for Information Technology–Telecommunications and Information Exchange Between Systems Local and Metropolitan Area Networks–Specific Requirements Part 11: Wireless LAN Medium Access Control (MAC) and Physical Layer (PHY) Specifications Amendment 2: Enhanced Throughput for Operation in License-Exempt Bands Above 45 GHz*, IEEE Standard 802.11ay-2021 (Amendment to IEEE Standard 802.11-2020 as amendment by IEEE Standard 802.11ax-2021), pp. 1–768, 2021.

[13] C. Chen, H. Song, Q. Li, F. Meneghello, F. Restuccia, and C. Cordeiro, "Wi-Fi sensing based on IEEE 802.11bf," *IEEE Commun. Mag.*, to be published, doi: 10.1109/MCOM.007.2200347.

[14] M. Cherniakov, *Bistatic Radar: Emerging Technology*. New York, NY, USA: Wiley, Inc., 2008.

[15] N. J. Willis and H. D. Griffiths, *Advances in Bistatic Radar*, SciTech Publishing, Raleigh, NC, 2007.

[16] M. A. Richards, J. Scheer, W. A. Holm, and W. L. Melvin, *Principles of Modern Radar*, vol. 1. Princeton, NJ, USA: Citeseer, 2010.

[17] V. Kostylev, *Geometry of Bistatic Radars*. New York, NY, USA: Wiley, ch. 11, pp. 225–241, 2007.

[18] H. D. Griffiths, ed., *Advances in Bistatic Radar. Radar, Sonar and Navigation*. London, England: Institution of Engineering and Technology, 2007.

[19] *IEEE Standard for Information Technology–Telecommunications and Information Exchange Between Systems - Local and Metropolitan Area Networks–Specific Requirements - Part 11: Wireless LAN Medium Access Control (MAC) and Physical Layer (PHY) Specifications*, IEEE Standard 802.11-2020 (Revision of IEEE Standard 802.11-2016), 2021.

[20] H. Assasa, "WiGig tools," 2022. [Online]. Available: https://github.com/wigig-tools

[21] S. Blandino, T. Ropitault, A. Sahoo, and N. Golmie, "Tools, models and dataset for IEEE 802.11ay CSI-based sensing," in *Proc. IEEE Wireless Commun. Netw. Conf.*, pp. 662–667, 2022.

[22] M. Lecci et al., "Simplified ray tracing for the millimeter wave channel: A performance evaluation," in *Proc. IEEE Inf. Theory Appl. Workshop*, 2020, pp. 1–6.

[23] S. Blandino, "Integrated sensing and communication physical layer model." 2022. [Online]. Available: https://github.com/wigig-tools/isac-plm

[24] J. Zhang, S. Blandino, N. Varshney, J. Wang, C. Gentile, and N. Golmie, "Multi-user MIMO enabled virtual reality in IEEE 802.11ay WLAN," in *Proc. IEEE Wireless Commun. Netw. Conf.*, 2022, pp. 2595–2600.

[25] R. Boulic, N. Magnenat-Thalmann, and D. Thalmann, "A global human walking model with real-time kinematic personification," *Vis. Comput.*, vol. 6, pp. 344–358, Nov. 1990.

STEVE BLANDINO received the M.Sc. degree in telecommunications engineering from Politecnico di Torino, Turin, Italy, and Telecom Paris Tech, Paris, France, in 2015, and the Ph.D. degree in electrical engineering from the Katholieke Universiteit Leuven, Leuven, Belgium, in 2019. In 2019, he joined the National Institute of Standard and Technology, Gaithersburg, MD, USA, as a Guest Researcher with the Wireless Network Division. He is currently a Contractor with the same division. His research interests include integrated sensing and communication signal processing, millimeter-wave and sub-THz communications, and channel modeling.

TANGUY ROPITAULT received the Ph.D. degree in computer science from Institut Mines-Telecom, Rennes, France, in 2015. He is currently a Contractor with the Wireless Network Division, National Institute of Standards and Technology, Gaithersburg, MD, USA. His research interest include mmWave and Wi-Fi sensing system-level performance evaluation.

CLAUDIO R. C. M. DA SILVA (Senior Member, IEEE) received the B.S. and M.S. degrees in electrical engineering from the State University of Campinas, Campinas, Brazil, in 1999 and 2001, respectively, and the Ph.D. degree in electrical engineering from the University of California, San Diego, CA, USA, in 2005. He is currently a Wireless Systems Engineer with the Reality Labs Group of Meta Platforms (formerly Facebook) and responsible for the standardization of wireless connectivity technologies and for advancing Meta's spectrum policy strategy. He is the Technical Editor of IEEE 802.11bf (WLAN Sensing), a task group currently developing an IEEE 802.11 amendment that enhances Wi-Fi sensing technology, and an IEEE ComSoc Distinguished Lecturer during 2022–2023. Before joining Meta Platforms, he was with the Next Generation and Standards Group of Intel Corporation, where he was responsible for driving technology and product innovation by leading and contributing to various standardization, certification, and regulatory activities. During his tenure at Intel, he was the Technical Editor of Wi-Fi Alliance's 60 GHz TTG from 2019 to 2021. Before Intel, he was on cellular modem implementation and applied research with Samsung Mobile Solutions Lab. The first years of his professional career were spent with Virginia Tech, Blacksburg, VA, USA, where he was an Assistant Professor with the Bradley Department of Electrical and Computer Engineering. He was the Editor of Modulation and Signal Design for the IEEE TRANSACTIONS ON COMMUNICATIONS from 2012 to 2015, and was on the technical program committee of numerous IEEE conferences in the communications area.

ANIRUDHA SAHOO (Senior Member, IEEE) received the Ph.D. degree in computer science from Texas A&M University, College Station, TX, USA. He was a Software Engineer with Intergraph Corporation, Huntsville, AL, USA, and Senior Software Engineer with Cisco Systems, San Jose, CA, USA. He was an Associate Professor with the Computer Science and Engineering Department, IIT Bombay, Bombay, India. He is currently a Computer Scientist with the National Institute of Standards and Technology, Gaithersburg, MD, USA. His research interests include spectrum sharing, dynamic spectrum access, and next generation wireless networks.

NADA GOLMIE (Fellow, IEEE) received the Ph.D. degree in computer science from the University of Maryland, College Park, MD, USA. Since 1993, she has been a Research Engineer with the National Institute of Standards and Technology (NIST), Gaithersburg, MD, USA. From 2014 to 2022, she was the Chief of Wireless Networks Division with NIST. She is currently a NIST Fellow with the Communications Technology Laboratory. She is the Author of *Coexistence in Wireless Networks: Challenges and System-level Solutions in the Unlicensed Bands*, published by Cambridge University Press in 2006. Her research interests include media access control and protocols for wireless networks led to more than 200 technical papers presented at professional conferences, journals, and contributed to international standard organizations and industry led consortia. She leads several Projects related to the modeling and evaluation of future generation wireless systems and protocols and the NextG Channel Model Alliance chair.